

Multi-Scale Thermal to Visible Face Verification via Attribute Guided Synthesis

Xing Di, *Student Member, IEEE* and Benjamin S. Riggan, *Member, IEEE* and Shuowen Hu, *Member, IEEE* and Nathaniel J. Short, *Member, IEEE* Vishal M. Patel, *Senior Member, IEEE*

Abstract—Thermal-to-visible face verification is a challenging problem due to the large domain discrepancy between the modalities. Existing approaches either attempt to synthesize visible faces from thermal faces or extract robust features from these modalities for cross-modal matching. In this paper, we use attributes extracted from visible images to synthesize the attribute-preserved visible images from thermal imagery for cross-modal matching. A pre-trained VGG-Face network is used to extract the attributes from the visible image. Then, a novel multi-scale generator is proposed to synthesize the visible image from the thermal image guided by the extracted attributes. Finally, a pre-trained VGG-Face network is leveraged to extract features from the synthesized image and the input visible image for verification. An extended dataset consisting of polarimetric thermal faces of 121 subjects is also introduced. Extensive experiments evaluated on various datasets and protocols demonstrate that the proposed method achieves state-of-the-art performance.

I. INTRODUCTION

Face Recognition (FR) is one of the most widely studied problems in computer vision and biometrics research communities due to its applications in authentication, surveillance and security. Various methods have been developed over the last two decades that specifically attempt to address the challenges such as aging, occlusion, disguise, variations in pose, expression and illumination. In particular, convolutional neural network (CNN) based FR methods have gained significant traction in recent years [32]. Deep CNN-based methods [29], [37], [44], [3], [32], [31], [4], [45] have achieved impressive performances on the current FR benchmarks.

Despite the success of CNN-based methods in addressing various challenges in FR, they are fundamentally limited to recognizing face images that are collected near-infrared spectrum. In many practical scenarios such as surveillance in low-light conditions, one has to detect and recognize faces that are captured using thermal modalities [16], [35], [39], [49], [34], [21], [28], [24], [2]. However, the performance of many deep learning-based methods degrades significantly when they are presented with thermal face images. For example, it was shown

Xing Di is with the Whiting School of Engineering, Johns Hopkins University, 3400 North Charles Street, Baltimore, MD 21218-2608, e-mail: xing.di@jhu.edu

Benjamin S. Riggan is with the University of Nebraska, e-mail: briggan2@unl.edu

Shuowen Hu is with the U.S. Army Combat Capabilities Development Command (CCDC) Army Research Laboratory (ARL), e-mail: shuowen.hu.civ@mail.mil

Nathaniel J. Short is with Booz Allen Hamilton, e-mail: short_nathaniel@bah.com

Vishal M. Patel is with the Whiting School of Engineering, Johns Hopkins University, e-mail: vpatel36@jhu.edu

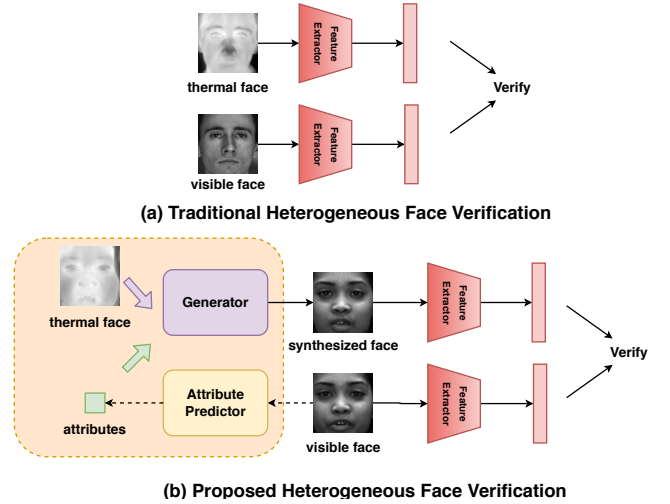


Fig. 1: (a) Traditional heterogeneous face verification approaches use the features directly extracted from different modalities for verification [15], [21], [18], [42]. (b) The proposed heterogeneous face verification approach uses a thermal face and semantic attributes to synthesize a visible face. Then, deep features extracted from the synthesized and visible faces are used for verification.

in [49], [34], [7], [6] that simply using deep features extracted from both thermal and visible facial images are not sufficient enough for cross-domain face recognition. The performance degradation is mainly due to the significant distributional change between the thermal and visible domains as well as a lack of sufficient data for training the deep networks for cross-modal matching.

Several attempts have been made to address the thermal-to-visible cross-spectrum face recognition problem [34], [35], [49], [7], [50]. For instance, Riggan *et al.*[35] proposed a two-step procedure (visible feature estimation and visible image reconstruction) to solve this cross-modal matching problem. Zhang *et al.*[49] proposed an end-to-end generative adversarial network by fusing the different Stokes images as a multi-channel input to synthesize the visible image given the corresponding polarimetric signatures. Recently, Riggan *et al.*[34] developed a global and local region-based technique to improve the discriminative quality of the synthesized visible imagery. Zhang *et al.*[50] introduced a multi-stream feature-level fusion method to synthesize high-quality visible images from polarimetric thermal images. Though these methods are able to synthesize photo-realistic visible face images to some

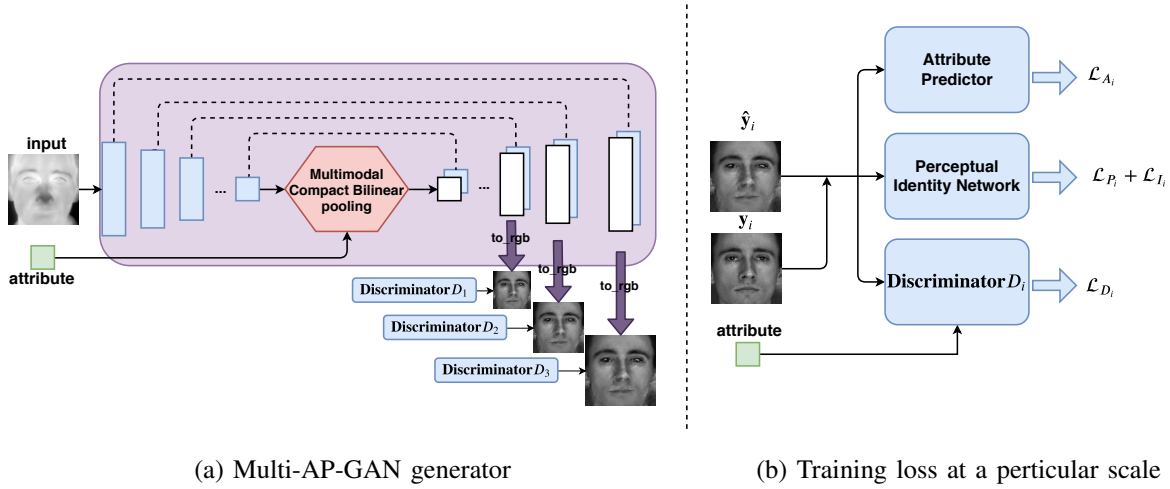


Fig. 2: (a) A single generator with multi-scale resolution output is proposed to synthesize high-quality images by leveraging hierarchical information at different scales. Multimodal Bilinear Pooling (MCB) pooling is proposed to fuse the semantic attribute information with the image feature in the latent space. (b) In order to make sure that the synthesized image maintains the identity and semantic attributes, a multi-purpose objective function is adopted which consists of adversarial loss \mathcal{L}_{D_i} , \mathcal{L}_1 loss, perceptual loss \mathcal{L}_{P_i} , identity loss \mathcal{L}_{I_i} and attribute preserving loss \mathcal{L}_{A_i} .

extent, the synthesized results in [49], [33], [34] are still far from optimal and they tend to lose some semantic attribute information such as expression, facial hair, gender, etc. Such reconstructions may degrade the performance of thermal-to-visible face verification.

In this paper, we take a different approach to the problem of thermal-to-visible matching. Fig. 1 compares the traditional cross-modal verification problem with that of the proposed attribute-preserved cross-modal verification approach. Given a visible and thermal image pair, the traditional approach first extracts some features from these images and then verifies the identity based on the extracted features [21] (see Fig. 1(a)). In contrast, we propose a novel framework in which we make use of the attributes extracted from the visible image to synthesize the attribute-preserved visible image from the input thermal image for matching (see Fig. 1(b)). In particular, a pre-trained VGG-Face model [29] is used to extract the attributes from the visible image. Then, a novel Multi-Scale Attribute Preserved Generative Adversarial Network (Multi-AP-GAN) is proposed to synthesize the visible image from the thermal image guided by the extracted attributes. Finally, a deep network is used to extract features from the synthesized and the input visible images for verification.

The proposed Multi-AP-GAN model is inspired by the recent works [23], [54], [47], [56], [55], in which deep supervision [23] is used at intermediate convolutional layers to learn better feature representations. Specifically, the Multi-AP-GAN consists of two parts: (i) a multimodal compact bilinear (MCB) pooling-based generator [8], [9], and (ii) a generator with the multi-scale architecture. The MCB pooling module fuses the given attributes with the image features. The multi-scale architecture aims to improve the synthesis image quality by leveraging hierarchical representations of CNNs at different image resolutions.

Fig. 2 gives an overview of the proposed Multi-AP-GAN

framework. A single generator with a series of distinct discriminators are employed to learn the multi-scale adversarial discrimination at different scales [43]. The generator fuses the extracted attribute vector with the image feature vector in the latent space. On the other hand, each discriminator uses triplet pairs (real image/true attributes, fake image/true attributes, fake image/wrong attributes) to not only discriminate between real and fake images but also to discriminate between the image and the attributes. In order to generate high-quality and attribute-preserved images, the generator is optimized by a multi-purpose objective function consisting of adversarial loss [10], L_1 loss, perceptual loss [19], identity loss [49] and attribute preserving loss.

To summarize, this paper makes the following contributions:

- We propose a novel thermal-to-visible face verification framework in which Multi-AP-GAN is developed for synthesizing high-quality visible faces from thermal images guided by facial attributes.
- We propose a single generator with a multi-scale output architecture and a Multimodal Compact Bilinear (MCB) pooling module [8], [9] to generate high-quality visible images.
- A novel triplet-pair discriminator is proposed, where the discriminator [33] not only learns to discriminate between real/fake images as well as images/visual-attributes.
- An extended version of the ARL polarimetric thermal face database consisting of data from 121 individuals is introduced in this work.
- Extensive experiments are conducted on three different volumes of the ARL Multimodal Facial Database [16], [50] as well as the Thermal and Visible Paired Face Database [26], and comparisons are performed against several recent state-of-the-art approaches. Furthermore, an ablation study is conducted to demonstrate the improvements obtained by including semantic attribute in-

formation for synthesis.

Note that the proposed Multi-AP-GAN framework can be viewed as an extended version of our earlier paper in the 2018 BTAS proceeding [7]. However, the generators used in both papers are quite different. The generator in [7] is a single-scale generator whereas a multi-scale generator is proposed in this paper. Furthermore, a new polarimetric thermal face dataset consisting of multi-modal data from 121 subjects is introduced in this paper. Extensive experiments and analysis are presented using the new dataset as well as the Thermal and Visible Paired Face Database [26].

Rest of the paper is organized as follows. In Section II, we review a few related works on visible to thermal face synthesis and matching. Details of the proposed Multi-AP-GAN method are given in Section III. Datasets and corresponding protocols are described in Section IV. Experimental results are presented in Section V. Finally, Section VI concludes the paper with a brief summary and discussion.

II. RELATED WORK

In this section, we review some related works on thermal-to-visible face synthesis and recognition.

A. Feature-based Thermal-Visible Face Recognition

As described in Fig. 1, traditional thermal-to-visible face verification methods first extract features from the visible and thermal images and then verify the identity based on the extracted features. Both hand-crafted and learned features have been investigated in the literature. Hu *et al.*[15] proposed a partial least squares (PLS) regression-based approach for cross-modal matching. Klare *et al.*[22] developed a generic framework for heterogeneous face recognition based on kernel prototype nonlinear similarities. Another multiple texture descriptor fusion-based method was proposed by Bourlai *et al.* in [42] for cross-modal face recognition. In [18] PLS-based discriminant analysis approaches were used to correlate the thermal face signatures to the visible face signatures. He *et al.*[14], [13], [46] introduced several high-level representation-learning based methods to disentangle feature representations into domain-invariant identity representation and domain-related spectrum representation. Some of the other visible to thermal cross-modal matching methods include [11], [38], [40].

B. Synthesis-based Thermal-Visible Face Recognition

Unlike the above mentioned traditional methods, synthesis-based thermal-to-visible face verification algorithms leverage the synthesized visible faces for verification. Due to the success of CNNs and recently introduced generative adversarial networks (GANs) in synthesizing realistic images, various deep learning-based approaches have been proposed in the literature for thermal-to-visible face synthesis [34], [49], [53], [35], [12], [48]. For example, Riggan *et al.*[35] proposed a two-step procedure (visible feature estimation and visible image reconstruction) to solve the thermal-to-visible verification problem. Zhang *et al.*[49] proposed an end-to-end GAN-based

approach for synthesizing photo-realistic visible face images from their corresponding polarimetric images. Recently Riggan *et al.*[34] proposed a new synthesis method to enhance the discriminative quality of generated visible face images by leveraging both global and local facial regions. Zhang *et al.*[50] introduced a multi-stream fusion-based generative model for cross-modal verification. Di *et al.*[7] proposed a GAN-based network called, AP-GAN to improve the synthesized visible image by utilizing visual attributes. Di *et al.*[6] proposed another unsupervised generative model which combines features from both thermal-to-visible and visible-to-thermal synthesized images for cross-modal verification. He *et al.*[12] proposed a generative model for thermal-to-visible face synthesis by utilizing texture inpainting and pose correction.

III. PROPOSED METHOD

In this section, we discuss details of the proposed Multi-AP-GAN method (see Fig. 2). In particular, we discuss the proposed attribute predictor, multi-scale generator and a series of distinct accompanying discriminators as well as the loss function used to train these networks.

A. Attribute Predictor

To efficiently extract attributes from a given visible face, an attribute predictor is fine-tuned based on the public VGG-Face network [29] using the annotated attributes. This network is trained separately from Multi-AP-GAN. The fine-tuned network is used in both obtaining the visible face attributes and for capturing the attribute loss when training the generator and discriminator. When fine-tuning the network, a binary cross-entropy loss is used and the final fully-connected layer has the same dimension as the number of visual attributes.

B. Generator

A U-net structure [36] is used as the building block for the multi-scale generator since it is able to better capture large receptive field and also able to efficiently address the vanishing gradient problem. In addition, to effectively combine the extra facial attribute information into the building block, we fuse the attribute vector and the image feature in the latent space [33], [49], [5]. Note that the attributes are extracted from the given visible face using the fine-tuned model as discussed above. The generator architecture is illustrated in Fig 3(a).

In our experiments, we observe that simple concatenation of the two vectors (encoded image vector and attribute vector) does not work well. One possible reason is that both vectors are significantly different in terms of their dimensionality. Thus, we adopt the well-known MCB pooling method [8], [9] to overcome this issue. Instead of simple concatenation, MCB leverages the following two techniques: bilinear pooling and sketch count. Bilinear pooling is the outer-product and linearization of two vectors, where all elements of both vectors are interacting with each other in a multiplicative way. In order to overcome the high-dimension computation of bilinear pooling, Pham *et al.*[30] implemented the count sketch of the outer product of two vectors, which involves the Fast

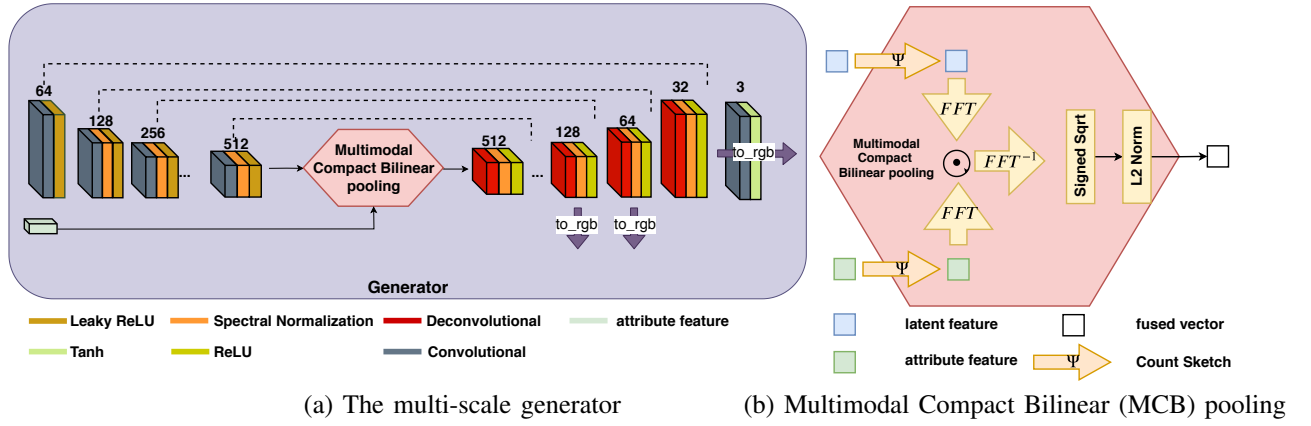


Fig. 3: The network architecture of multi-scale generator and multimodal compact bilinear (MCB) pooling in details.

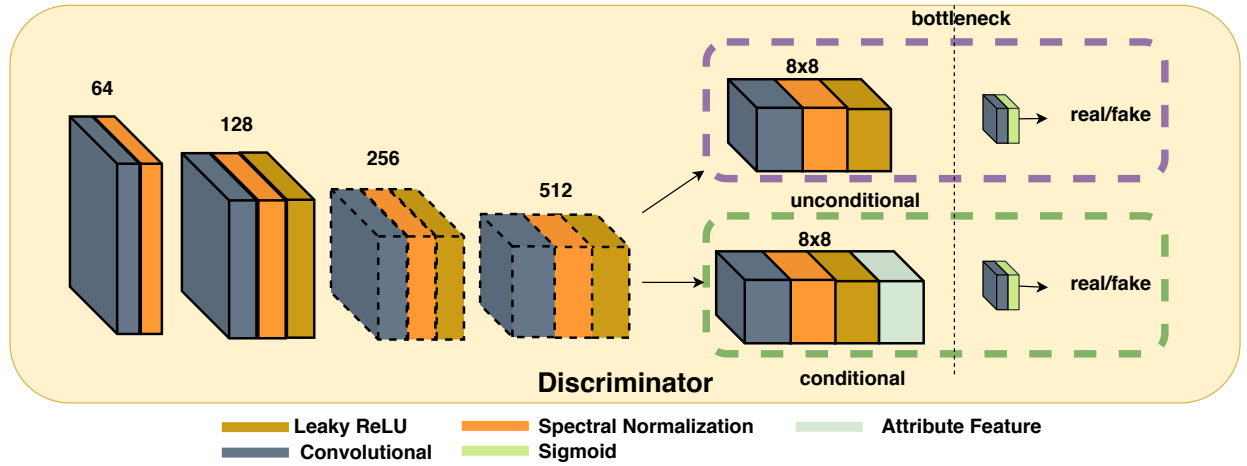


Fig. 4: An illustration of the certain 256×256 triplet-pair-input discriminator. The triplet-pair-input discriminator is composed of a conditional and an unconditional streams. The unconditional stream aims to discriminate the fake and real images. The conditional stream aims to discriminate between the image and the corresponding attributes. In order to keep the bottleneck feature map size to be consistent to 8×8 for different input image resolution scale, a different number of downsampling layers (dash-line green cubic) are utilized.

Fourier Transform (FFT) and inverse Fast Fourier Transform (FFT^{-1}). The architecture of MCB module is shown in Fig 3(b).

In order to improve the quality of the synthesized visible images, the proposed single generator utilizes a multi-scale output architecture. Specifically, the generator G produces multiple outputs at different resolution scales as follows

$$G(\mathbf{x}, \mathbf{z}) = \{\hat{\mathbf{y}}_1, \dots, \hat{\mathbf{y}}_s\}, \quad (1)$$

where \mathbf{x}, \mathbf{z} denote the input thermal image and the extracted visual-attributes, respectively. Here, $\{\hat{\mathbf{y}}_1, \dots, \hat{\mathbf{y}}_s\}$ denote the synthesized images with gradually growing resolutions and $\hat{\mathbf{y}}_s$ is the final output with the highest resolution s . In this work, we set $s = 3$. These multi-scale resolution outputs act as a regularizer to the generator G . Furthermore, they shorten the error signal flow path and help to improve the training stability [55].

The multi-scale generator network, as shown in Fig. 3(a), consists of the following components:

CL(64)-CNL(128)-CNL(256)-CNL(512)-CNL(512)-

CNL(512)-CNL(512)-MCB(512)-DNR(512)-DNR(512)-DNR(512)-DNR(256)-DNR(128)-DNR(64)-DNR(32), where C stands for the convolutional layer (stride 2, kernel-size 4, and padding-size 1), L stands for Leaky Relu layer (negative_slope=0.02), N stands for the spectral-normalization layer [27], MCB indicates the Multimodal Compact Bilinear module [8], [9], D stands for the deconvolutional layer (stride 2, kernel-size 4 and padding-size 1), and R corresponds to the ReLU layer. All the numbers in parenthesis indicate the channel number of the output feature maps. Note that we add "to_rgb" blocks in the last 3 ($s = 3$) "DBR" blocks to convert the feature maps into 3-channel images. A "to_rgb" block consists of two standard 1×1 convolutional layers followed a Tanh layer.

C. Discriminator

A series of distinct discriminators $D_i, i = 1, \dots, s$ are utilized and trained iteratively with the generator G . For a certain discriminator at the i -th resolution scale, a patch-based discriminator [17] is leveraged and it not only aims to

discriminate between real/fake images but also to discriminate between the image and the corresponding attributes. Similar to previous works [33], [51], [55], a triplet of paired image and attribute is given to the discriminator: *real*, *fake* and *wrong*. The *real* pair consists of a real-image (\mathbf{y}_i) along with the corresponding true-attributes (\mathbf{z}). The *wrong* pair consists of a real image (\mathbf{y}_i) along with wrong attributes (\mathbf{z}'). The *fake* pair consists of a fake-image ($\hat{\mathbf{y}}_i$) with true attributes (\mathbf{z}). The overall adversarial objective function used to train the network is as follows:

$$\begin{aligned}\mathcal{L}_G &= \sum_{i=1}^s \min_G \max_{D_i} (V_{real}^i + V_{fake}^i + V_{wrong}^i), \\ V_{real}^i &= \mathbb{E}_{\mathbf{y}_i \sim P_Y} [\log D_i(\mathbf{y}_i)] \\ &\quad + \mathbb{E}_{\mathbf{y}_i, \mathbf{z} \sim P_{Y,Z}} [\log D_i(\mathbf{y}_i, \mathbf{z})] \\ V_{wrong}^i &= \mathbb{E}_{\mathbf{y}_i, \mathbf{z}' \sim P_{Y,Z}} [\log(1 - D_i(\mathbf{y}_i, \mathbf{z}'))] \\ V_{fake}^i &= \mathbb{E}_{\hat{\mathbf{y}}_i \sim P_{G(\mathbf{x}, \mathbf{z})}} [\log(1 - D_i(\hat{\mathbf{y}}_i))] \\ &\quad + \mathbb{E}_{\hat{\mathbf{y}}_i \sim P_{G(\mathbf{x}, \mathbf{z})}, \mathbf{z} \sim P_Z} [\log(1 - D_i(\hat{\mathbf{y}}_i, \mathbf{z}))].\end{aligned}\quad (2)$$

Specifically, each discriminator D_i has two streams: conditional stream and unconditional stream. One discriminator on 256×256 resolution scale is illustrated in Fig. 4. The unconditional stream aims to learn the discrimination between the real and the synthesized images. This unconditional adversarial loss is back-propagated to G to make sure that the generated samples are as realistic as possible. In addition, the conditional stream aims to learn whether the given image matches the given attributes or not. This conditional adversarial loss is back-propagated to G so that it generates samples that are attribute-preserving.

Fig. 4 gives an overview of a discriminator at 256×256 resolution scale. This discriminator consists of 6 convolutional blocks for both conditional and unconditional streams. Details of these convolutional blocks are as follows: CL(64)-CNL(128)-CNL(256)-CNL(512)-C[†]NL(512)-C[†]S(1), where S stands for the Sigmoid activation layer. Note that the only difference between the unconditional and conditional stream is the concatenation of the attribute vector at the fifth convolutional block. For different discriminator D_i at different resolution scale, the number of convolutional down-sample blocks (blocks with dotted lines in Fig. 4) vary, but we keep the bottleneck feature map at the same size (i.e. 8×8). The architecture details corresponding to the other discriminators are given in Table I.

D. Object Function

The generator is optimized by minimizing the following loss

$$\mathcal{L}_{Multi-AP-GAN} = \mathcal{L}_G + \lambda_A \mathcal{L}_A + \lambda_P \mathcal{L}_P + \lambda_I \mathcal{L}_I + \lambda_1 \mathcal{L}_1, \quad (3)$$

where \mathcal{L}_G is the multi-scale adversarial loss in Eq (2), \mathcal{L}_P is the perceptual loss, \mathcal{L}_I is the identity loss, \mathcal{L}_A is the attribute loss, \mathcal{L}_1 is the loss based on the L_1 -norm between the target and the reconstructed image, and $\lambda_P, \lambda_I, \lambda_A, \lambda_1$ are the corresponding weights.

[†]unconditional and conditional streams are shorten for brief.

TABLE I: Architecture details corresponding to different discriminators. Numbers in parenthesis indicate the channel number of the output feature maps. The convolutional layers have stride size 2.

Discriminator 64x64	Discriminator 128x128	Discriminator 256x256
Convolutional (64) LeakyReLU	Convolutional (64) LeakyReLU	Convolutional (64) LeakyReLU
Convolutional (128) Spectral Norm LeakyReLU	Convolutional (128) Spectral Norm LeakyReLU	Convolutional (128) Spectral Norm LeakyReLU
Convolutional [†] (256) Spectral Norm LeakyReLU	Convolutional (256) Spectral Norm LeakyReLU	Convolutional (256) Spectral Norm LeakyReLU
Convolutional [†] (1) Sigmoid	Convolutional [†] (512) Spectral Norm LeakyReLU	Convolutional (512) Spectral Norm LeakyReLU
	Convolutional [†] (1) Sigmoid	Convolutional [†] (512) Spectral Norm LeakyReLU
		Convolutional [†] (1) Sigmoid

1) *Multi-scale Perceptual and Identity Loss*: Perceptual loss was originally introduced by Johnson *et al.*[19] for style transfer and super-resolution. It has been observed that the perceptual loss produces visually pleasing results than L_1 or L_2 loss. The perceptual and identity losses are defined as follows

$$\mathcal{L}_{P,I} = \sum_{i=1}^s \sum_{c=1}^3 \sum_{w=1}^W \sum_{h=1}^H \|F(\hat{\mathbf{y}}_i)^{c,w,h} - F(\mathbf{y}_i)^{c,w,h}\|_1, \quad (4)$$

where F represents a non-linear CNN feature. VGG-16 [41] is used to extract features in this work. C, W, H are the dimensions of features from a certain level of the VGG-16, which are different for perceptual and identity losses. Since the deeper convolutional layer captures more semantic information, we choose deeper convolutional feature maps as the identity loss.

In addition, multi-scale L_1 loss between the synthesized image $\hat{\mathbf{y}}_i$ and the corresponding real image \mathbf{y}_i is used to capture the low-frequency information, which is defined as follows

$$\mathcal{L}_1 = \sum_{i=1}^s \|\hat{\mathbf{y}}_i - \mathbf{y}_i\|_1. \quad (5)$$

2) *Multi-scale Attribute Loss*: Inspired by the perceptual loss, we define an attribute preserving loss, which measures the error between the attributes of the synthesized image and the real image. To make sure the pre-trained model captures the facial attribute information, we fine-tune the pre-trained VGG-Face network on the annotated attribute dataset and regard the fine-tuned attribute classifier as the pre-trained model for the attribute preserving loss. Similar to the perceptual loss, the \mathcal{L}_A is defined as follows

$$\mathcal{L}_A = \sum_{i=1}^s \|Q(\hat{\mathbf{y}}_i) - Q(\mathbf{y}_i)\|_1, \quad (6)$$

where Q is the fine-tuned attribute predictor network. The output vectors are from the last layer as a result the feature dimensions C, W, H are omitted in (6). By feeding such

an attribute information into the generator during training, the generator G is able to learn semantic information corresponding to the face.

E. Implementation

The entire network is trained in Pytorch on a single Nvidia Titan-X GPU. During the Multi-AP-GAN training, the L_1 , perceptual and identity loss parameters are chosen as $\lambda_1 = 10$, $\lambda_P = 2.5$, $\lambda_I = 0.5$, respectively. The ADAM [20] is implemented as the optimization algorithm with parameter $\text{betas} = (0.5, 0.999)$ and batch size is set equal to 1. The total epochs are 200. For the first 100 epochs, we fix the learning rate as 0.0002 and for the remaining 100 epochs, the learning rate was decreased by $1/100$ after each epoch. The feature maps for the perceptual and the identity loss are from the relu1-1 and the relu2-2 layers, respectively. In order to fine-tune the attribute predictor network, we manually annotate images with the attributes tabulated in Table II.

TABLE II: The facial attributes used in this work.

attributes	Arched_Eyebrows, Big_Lips, Big_Nose, Bushy_Eyebrows, Male, Mustache, Narrow_Eyes, No_Beard, Mouth_Slightly_Open, Young
------------	--

IV. DATASETS AND PROTOCOLS

In this section, we describe the datasets and the protocols that we use to conduct experiments. In particular, we describe the new extended ARL Polarimetric thermal face dataset and the corresponding protocol that we use in this paper.

A. Extended Polarimetric Thermal Face Dataset

In many recent approaches, the polarization-state information of thermal emissions has been used to achieve improved cross-spectrum face recognition performance [16], [35], [39], [49], [34] since it captures geometric and textural details of faces that are not present in the conventional thermal facial images [39], [16]. A polarimetric thermal image consists of three Stokes images: S_0 , S_1 , S_2 where S_0 indicates the conventional total intensity thermal image, S_1 captures the horizontal and vertical polarization-state information, S_2 captures the diagonal polarization-state information [16]. Similar to [49], [34], we also refer to Polar as the three channel polarimetric image concatenated with S_0 , S_1 and S_2 . These Stokes images along with the visible and the polarimetric images corresponding to a subject in the ARL dataset [16] are shown in Fig. 5. It can be observed that S_1 , S_2 tend to preserve more textural details compared to S_0 .

The U.S. Army CCDC Army Research Laboratory (ARL) multimodal face dataset consists of polarimetric thermal and visible face image pairs in three volumes. Volume I consists of the polarimetric thermal and visible images from 60 subjects, which were collected by the U.S. Army Research Laboratory in 2014-2015. Frontal imagery with different ranges and expressions are included. Details regarding this volume can be found in [16] and [50]. Volume II consists of images from 51 subjects

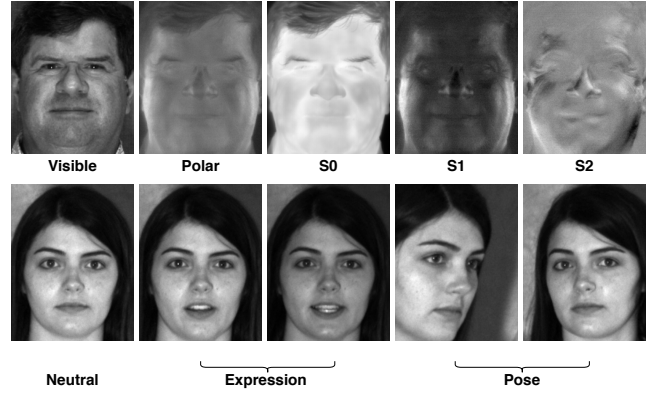


Fig. 5: Row 1: Left to right, example visible, polarimetric thermal, and Stokes images of a subject in the ARL dataset [16]. Row 2: Samples from Volume III with different neutral, expression and pose variations.

collected at a Department of Homeland Security test facility. As described in [50], while the participants of the Volume I subset consisted exclusively of the ARL employees, the participants of the Volume II collect were recruited from the local community in Maryland, resulting in more demographic diversity. In addition, frontal imagery with various expressions are included in this volume.

In this paper, we present an extension of the dataset which was collected by ARL across 11 different sessions over 6 days. We refer to this extended dataset as Volume III hereinafter. Volume III contains polarimetric thermal and visible facial signatures from 121 subjects collected at Johns Hopkins University Applied Physics Laboratory as part of an IARPA government testing event. There are a total of 5419 polarimetric thermal and visible image pairs with significant variations (Fig. 5) such as expression, off-pose, glasses, etc. These variations make the dataset more challenging for cross-modal face verification. Note that this extended database is available upon request.

To be consistent with previous methods [50], [16], the experimental protocols are defined as follows:

Protocol I: The Protocol I is evaluated on Volume I, which consists of frontal imagery with range and expression variations (including neutral expression). Images from 30 subjects with eight samples for each subject are used as the training split. Images from the other 30 subjects with eight samples for each subject are used as the test split. All the samples in training and test split are randomly chosen from 60 subjects. Results are evaluated on five random splits. Note that there are no overlapping subjects between training and test splits.

Protocol II: The Protocol II is evaluated on the extended 111 subject dataset which contains the images from both Volume I and Volume II. In particular, 85-subject images are used as the training split and the other 26-subject images are denoted as the test split. The 85-subject images in training split consist of all 60-subject images in Volume I and another 25-subject images randomly selected from Volume II. The other 26-subject images in Volume II are selected as the test split. As before, results are evaluated on five random splits [50]. Note

that Volume II consists of frontal imagery with expression variations only (including neutral expression).

Protocol III: The Protocol III is evaluated only on the Volume III data consisting of images from 121 subjects. Volume III includes frontal and off-pose imagery (excludes extreme pose, e.g. profile), and expression variation (including neutral expression). Images from 96 randomly chosen subjects are used as the training split and the images from the remaining 25 subjects are used as the test split. Results are evaluated on five random splits.

B. Visible and Thermal Paired Face Database

In addition to the ARL dataset, the proposed method is evaluated on a recently introduced Visible and Thermal Paired Face Database [26]. This dataset contains thermal and visible image pairs corresponding to 50 subjects. Each subject participated in two different sessions separated by a time interval of 3 to 4 months. This dataset includes 21 face images per subject in each session. These images correspond to different facial variations in illumination, head pose, expression and occlusion. In total, 4200 images are included in this dataset.

Protocol: Images corresponding to randomly chosen 30 subjects are used as the training split and the images from the remaining 20 subjects are used as the test split. This results in 630 paired training images and 420 paired testing images. There is no overlap among subjects in the training and the test sets. Results are evaluated on five random splits.

C. Preprocessing

In addition to the standard preprocessing, two more preprocessing steps are used for the proposed method. First, the faces in the visible images are detected by MTCNN [52]. Then, a standard central crop method is used to crop the detected faces. Since MTCNN is implementable on the visible images only, we use the same detected rectangle coordinations to crop the thermal images, which were already aligned to the same canonical coordinates as the visible images. After preprocessing, all the images are scaled and saved as 256×256 16-bit PNG files.

D. Metrics

Once the visible image is synthesized from the input probe thermal image, we use a pre-trained VGG-Face model [29] to extract features from the synthesized visible probe image as well as the visible gallery image to perform cross-modal face verification. In particular, the verification score is calculated using the cosine similarity between the two feature vectors. The cross-modal verification performance of different methods is evaluated using the Receiver Operating Characteristic (ROC) curve, Area Under the Curve (AUC) and Equal Error Rate (EER) measures.

V. EXPERIMENTAL RESULTS

In this section, we demonstrate the effectiveness of the proposed approach by conducting various experiments on the datasets described in the previous section. Since the ARL

Dataset contains both conventional thermal (S_0) and polarimetric thermal modalities, we conduct the following two cross-modal face verification experiments on the ARL dataset: 1) Conventional thermal (S_0) to Visible (Vis) and 2) Polarimetric thermal (Polar) to Visible (Vis). On the other hand, the Visible and Thermal Paired Face Database does not contain polarimetric thermal images. As a result, we only conduct thermal-to-visible cross-domain face verification experiments on this dataset.

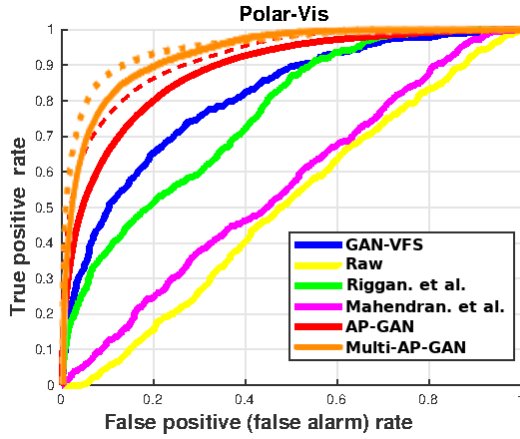
We evaluate and compare the performance of the proposed method with that of the following recent state-of-the-art methods [49], [25], [35], [34], [7], [50]. Note that our previous work [7] can be viewed as a single scale version of the proposed method. In particular, in [7], we synthesize images at a particular scale which has the same resolution as the input. We also conduct experiments with another baseline method called, Multi-AP-GAN (GT), where we use the ground-truth attributes in our method rather than automatically predicting them using the proposed attribute predictor. This baseline will clearly determine how effective the proposed attribute predictor is in determining the attributes from unconstrained visible faces.

A. Results on the ARL Face Dataset

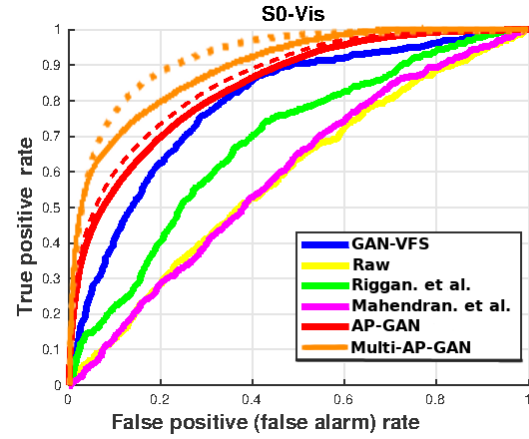
Fig. 6 shows the performance corresponding to Protocol I on two different experimental settings (i.e S_0 -to-visible and Polar-to-visible). Compared with other state-of-the-art methods in Fig. 6, the proposed method performs better with a larger AUC and lower EER scores. In addition, it can be observed that the performance corresponding to the Polar modality is better than the S_0 modality, which also demonstrates the advantage of using the polarimetric thermal images than the conventional thermal images. In addition, the gap between the results with ground-truth attributes (dash-line) and that with the predicted attributes (solid-line) demonstrate the degradation caused by the attribute predictor. The quantitative comparisons, as shown in the Table III, also demonstrate the effectiveness of the proposed method. In addition, compared with the previous single scale resolution method [7], the proposed multi-scale algorithm achieves significant improvement: around 4% and 6% on the conventional and polarimetric thermal modalities, respectively. These improvements demonstrate the effectiveness of the proposed multi-scale synthesis algorithm.

Furthermore, we also show some visual comparisons in Fig. 9. The first row in Fig. 9 shows one synthesized sample using S_0 . The second row shows the same synthesized sample using a polarimetric thermal image. It can be observed that results of Riggan *et al.*[35] do capture the overall face structure but it tends to lose some facial details. Results of Mahendran *et al.*[25] are poor compared to [35]. Results of Zhang *et al.*[49] are more photo-realistic but tend to lose some attribute information. The proposed Multi-AP-GAN not only generates photo-realistic images but also preserves attributes on the reconstructed images.

Fig. 7 and Table IV show the performance of different methods on Protocol II. These results also demonstrate the superiority of the proposed method. Note that the performance

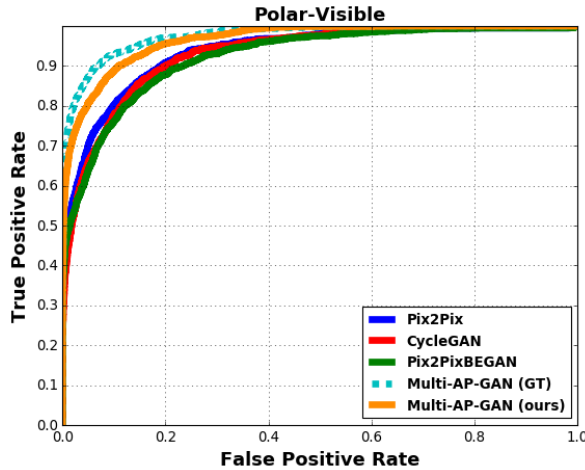


(a) Polarimetric thermal-to-visible verification

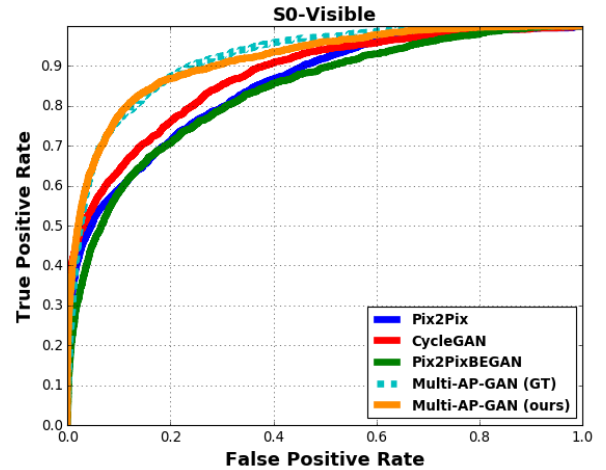


(b) Thermal-to-visible verification

Fig. 6: The ROC curve comparison on Protocol I with several state-of-the-art methods: (a) Polarimetric thermal-to-visible verification performance. (b) S0-to-Visible verification performance. Note that the dotted lines indicate results based on the ground-truth attributes. The gap between the results with ground-truth attributes and that with predicted attributes demonstrate the degradation caused by the attribute predictor.



(a) Polarimetric thermal-to-visible verification



(b) Thermal-to-visible verification

Fig. 7: The ROC curve comparison on Protocol II with several state-of-the-art methods: (a) Polarimetric thermal-to-visible verification performance. (b) S0-to-Visible verification performance. Note that the dotted lines indicate results based on the ground-truth attributes. The gap between the results with ground-truth attributes and that with predicted attributes demonstrate the degradation caused by the attribute predictor.

of many methods is slightly better in Protocol II than Protocol I. This is mainly due to the fact that the training dataset is larger in Protocol II than Protocol I.

Protocol III results corresponding to different methods are shown in Fig. 8 and Table V. Note that face images in this volume include many variations such as expression, pose, illuminations and occlusion (glasses). As a result, the performance of the methods compared is slightly lower than what we observed in Protocol I and Protocol II. In general, the proposed method performs favorably against the state-of-the-art methods. Note that Pix2PixBEGAN method [17], [1] fails to generate good quality visible faces from profile thermal face images. As a result, Pix2PixBEGAN method performs poorly on this dataset.

We further analyze the cross-modal verification performance

of different methods on different variation settings on Protocol III. The corresponding results are shown in Table VI. Since variations like occlusion and illumination are not included in some subjects, we only use three variations (neutral, expression, and pose) which are included in all subjects. As can be seen from Table VI, the performance degradation mainly comes from pose variations.

B. Results on the Visible and Thermal Paired Face Database

Table VII shows the performance of different methods on the Visible and Thermal Paired Face Database. Compared to the ARL dataset, the performance of every method is lower on this dataset. This is mainly due to the fact that this dataset is small in size and contains many facial variations. In general,

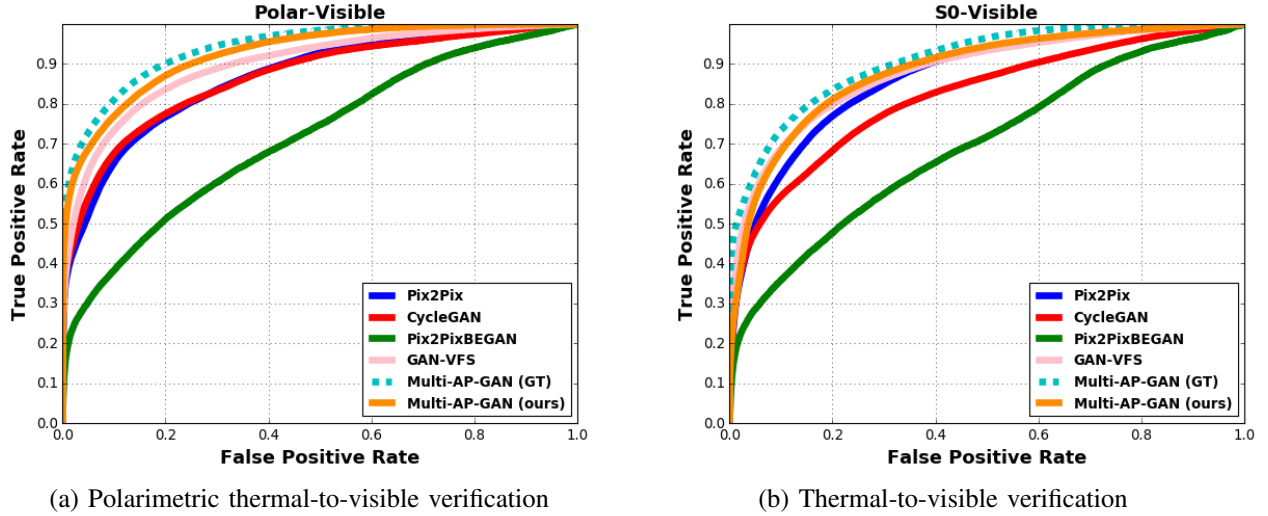


Fig. 8: The ROC curve comparison on Protocol III with several state-of-the-art methods: (a) Polarimetric thermal-to-visible verification performance. (b) S0-to-Visible verification performance. Note that the dotted lines indicate results based on the ground-truth attributes. The gap between the results with ground-truth attributes and that with predicted attributes demonstrate the degradation caused by the attribute predictor.

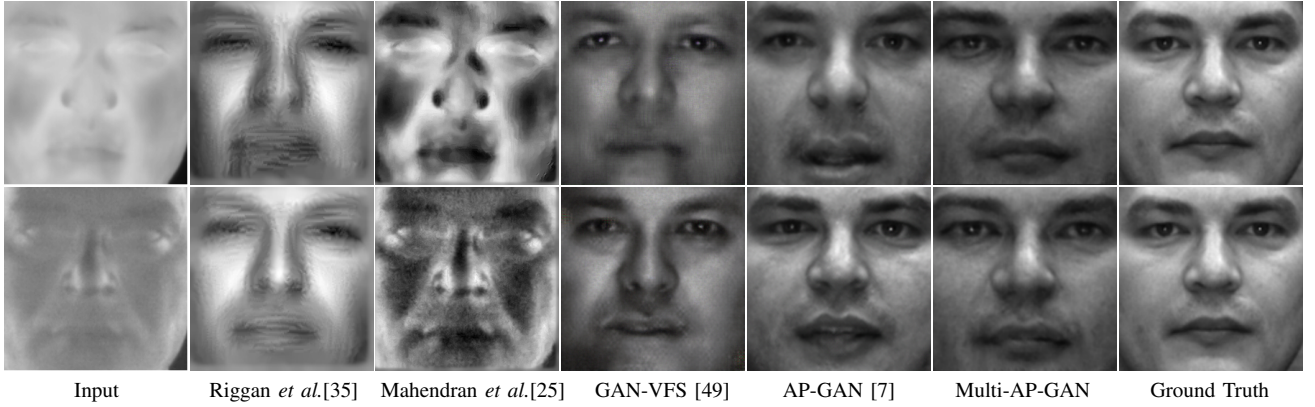


Fig. 9: The synthesized samples from different methods: Riggan *et al.*[35], Mahendran *et al.*[25], GAN-VFS [49], AP-GAN [7], Multi-AP-GAN, Ground Truth. The first row results correspond to the S0 image, and the second row results correspond to the Polar image.

the proposed method performs favorably against the previous methods.

In addition, following the analysis presented in [26], we also analyze how different variations (i.e. illumination, pose, expression, occlusion) influence the cross-spectrum matching performance of our method. As can be seen from the results in Table VIII illumination and pose variations are the two variations that affect the performance of our method the most. This analysis is based on the proposed method implemented with the ground-truth visual attributes.

We also show some visual results in Fig. 10. It can be observed that Pix2Pix [17] and CycleGAN [57] methods generate poor quality images with many artifacts. GAN-VFS *et al.*[49] is able to synthesize better quality images. However, this method also introduces some artifacts around the eyes and mouth regions. The proposed Multi-AP-GAN method not only generates photo-realistic images but also preserves attributes on the synthesized images. We also show some images in

Fig. 11 in which the proposed method is not able to produce good quality images. From these images we see that extreme pose, occlusion and illumination variations cause the proposed method to produce poor quality images.

C. Ablation Study

In order to demonstrate the effectiveness of different modules in the proposed method, we conduct the following ablation study using the Polarimetric thermal modality in the ARL dataset on Protocol I:

- 1) Polar to Visible estimation with only \mathcal{L}_1 (as defined in Eq. (5))
- 2) Polar to Visible estimation with \mathcal{L}_1 and \mathcal{L}_G (as defined in Eq. (2))
- 3) Polar to Visible estimation with \mathcal{L}_1 , \mathcal{L}_G , perceptual loss \mathcal{L}_P and identity loss \mathcal{L}_I , which are defined as in Eq. (4).

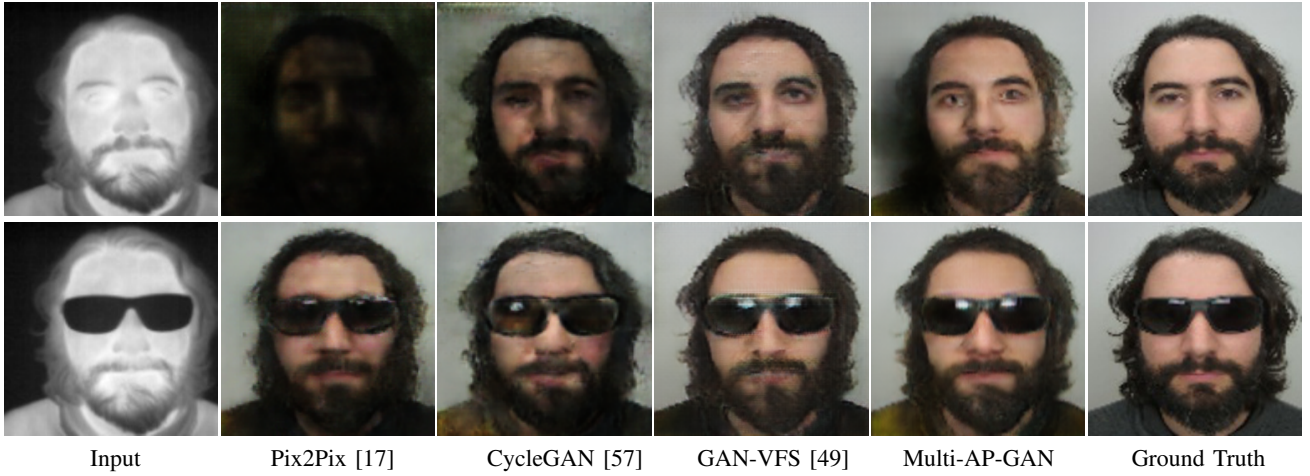


Fig. 10: The synthesized images corresponding to Pix2Pix[17], CycleGAN [57], GAN-VFS [49], Multi-AP-GAN (ours) from the Visible and Thermal Paired Face Database.



Fig. 11: Some failure cases. Note that extreme pose, illumination and occlusion variations cause the proposed method to synthesize poor quality images.

TABLE III: ARL Protocol I verification performance comparisons among the baseline methods, state-of-the-art methods, and the proposed Multi-AP-GAN method for both polarimetric thermal (Polar) and conventional thermal (S0) cases.

Method	AUC(Polar)	AUC(S0)	EER(Polar)	EER(S0)
Raw	50.35%	58.64%	48.96%	43.96%
Mahendran <i>et al.</i> [25]	58.38%	59.25%	44.56%	43.56%
Riggan <i>et al.</i> [35]	75.83%	68.52%	33.20%	34.36%
GAN-VFS <i>et al.</i> [49]	79.90%	79.30%	25.17%	27.34%
Riggan <i>et al.</i> [34]	85.43%	82.49%	21.46%	26.25%
AP-GAN [7]	88.93% \pm 1.54%	84.16% \pm 1.54%	19.02% \pm 1.69%	23.90% \pm 1.52%
AP-GAN (GT) [7]	91.28% \pm 1.68%	86.08% \pm 2.68%	17.58% \pm 2.36%	23.13% \pm 3.02%
Multi-stream GAN [50]	96.03%	85.74%	11.78%	23.18%
Multi-AP-GAN (ours)	93.61% \pm 1.46%	90.14% \pm 2.17%	14.24% \pm 1.91%	18.20% \pm 2.65%
Multi-AP-GAN (GT) (ours)	95.29% \pm 1.39%	92.72% \pm 2.03%	11.22% \pm 1.89%	16.05% \pm 2.15%

TABLE IV: ARL Protocol II verification performance comparisons among the baseline methods and the proposed method for both polarimetric thermal (Polar) and conventional thermal (S0) cases.

Method	AUC (Polar)	AUC(S0)	EER(Polar)	EER(S0)
Raw	66.85%	63.66%	37.85%	40.93%
Pix2Pix [17]	93.66% \pm 1.07%	85.09% \pm 1.48%	13.73% \pm 1.38%	23.12% \pm 1.14%
Pix2PixBEGAN [17], [1]	92.16% \pm 1.09%	83.69% \pm 1.28%	15.38% \pm 1.45%	26.22% \pm 1.16%
CycleGAN [57] (supervised)	93.11% \pm 1.02%	87.29% \pm 1.13%	15.19% \pm 1.02%	20.99% \pm 1.19%
Multi-stream GAN [50]	98.00%	—	7.99%	—
Multi-AP-GAN (ours)	96.55% \pm 1.12%	91.43% \pm 0.93%	10.17% \pm 1.01%	15.86% \pm 2.13%
Multi-AP-GAN (GT) (ours)	97.68% \pm 0.78%	91.88% \pm 0.87%	7.69% \pm 1.39%	15.29% \pm 2.36%

4) Polar to Visible estimation with all the losses $\mathcal{L}_{Multi-AP-GAN}$ as defined in Eq. (3).

Fig. 14 shows the ROC curves corresponding to each experimental setting. From this figure, we can observe that using all the losses together as $\mathcal{L}_{Multi-AP-GAN}$ can obtain the best performance. Compared to the results between \mathcal{L}_1

and $\mathcal{L}_1 + \mathcal{L}_G$, we can observe the enhancement provided by adding the adversarial loss. Compared with the results between $\mathcal{L}_1 + \mathcal{L}_G$ and $\mathcal{L}_1 + \mathcal{L}_G + \mathcal{L}_P + \mathcal{L}_I$, we can observe the improvements obtained by adding the perceptual and identity losses. On the other hand, one can clearly see the significance of fusing the semantic attribute information with the image

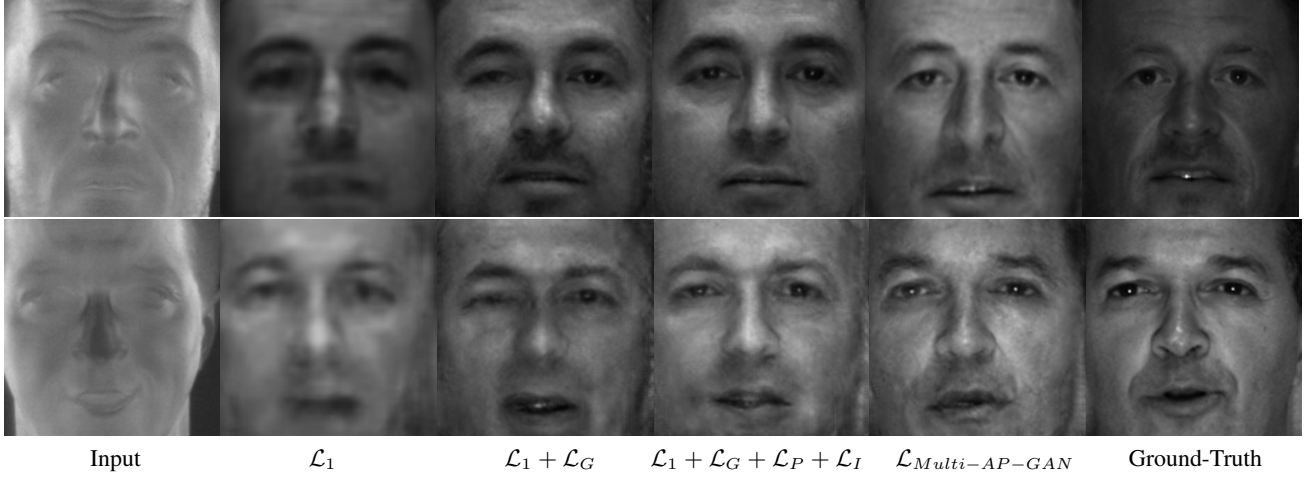


Fig. 12: The visual results of the ablation study for different experimental settings. Given input polarimetric thermal image, synthesized results using different combination of losses are shown successively from left to right.

TABLE V: ARL Protocol III verification performance comparisons among the baseline methods and the proposed method for both polarimetric thermal (Polar) and conventional thermal (S0) cases.

Method	AUC (Polar)	AUC(S0)	EER(Polar)	EER(S0)
Raw	73.43%	76.71%	33.56%	30.76%
Pix2Pix [17]	86.78% \pm 1.84%	86.65% \pm 1.48%	21.92% \pm 1.26%	23.12% \pm 1.77%
Pix2PixBEGAN [17], [1]	71.29% \pm 1.88%	69.42% \pm 1.84%	33.83% \pm 1.68%	36.88% \pm 1.76%
CycleGAN [57] (supervised)	86.77% \pm 1.77%	81.80% \pm 1.67%	21.48% \pm 1.11%	25.86% \pm 1.36%
GAN-VFS [†] [49]	90.20% \pm 1.85%	87.10% \pm 1.52%	18.53% \pm 1.21%	20.22% \pm 1.92%
Multi-AP-GAN (ours)	92.29% \pm 1.48%	88.49% \pm 1.87%	16.26% \pm 1.12%	19.25% \pm 1.62%
Multi-AP-GAN (GT) (ours)	93.72% \pm 1.08%	90.99% \pm 1.13%	14.75% \pm 1.36%	17.81% \pm 1.63%

TABLE VI: Protocol III verification performance with respect to different variations.

Variations	AUC (Polar)	AUC(S0)	EER(Polar)	EER(S0)
Neutral	96.77% \pm 1.25%	94.69% \pm 1.17%	12.50% \pm 2.09%	13.38% \pm 1.48%
Expression	96.77% \pm 1.91%	92.38% \pm 1.40%	10.05% \pm 2.02%	15.18% \pm 1.58%
Pose	86.62% \pm 2.39%	82.35% \pm 2.54%	22.45% \pm 1.84%	25.76% \pm 1.95%
Average	93.72% \pm 1.08%	90.99% \pm 1.13%	14.75% \pm 1.36%	17.81% \pm 1.63%

TABLE VII: Visible and Thermal Paired Face Database verification performance comparisons among the baseline methods and the proposed method for the conventional thermal case.

Method	AUC	EER
Raw	69.54%	35.39%
Pix2Pix [17]	78.66% \pm 1.48%	28.39% \pm 1.14%
Pix2PixBEGAN [17], [1]	73.69% \pm 1.82%	34.22% \pm 1.61%
CycleGAN [57] (supervised)	80.24% \pm 1.31%	26.72% \pm 1.39%
GAN-VFS [†] [49]	80.44% \pm 1.03%	26.33% \pm 1.19%
Multi-AP-GAN (ours)	81.73% \pm 0.93%	25.68% \pm 1.56%
Multi-AP-GAN (GT) (ours)	82.68% \pm 0.87%	23.16% \pm 0.98%

TABLE VIII: Verification performance with respect to different variations on the Visible and Thermal Paired Face Database.

Variations	AUC	EER
Illumination	73.35% \pm 0.25%	32.60% \pm 0.43%
Expression	97.25% \pm 0.68%	7.45% \pm 1.74%
Pose	78.25% \pm 1.03%	28.75% \pm 0.93%
Occlusion	83.98% \pm 1.33%	24.02% \pm 1.06%
Average	82.68% \pm 0.87%	23.16% \pm 0.98%

feature in the latent space by comparing the results between $\mathcal{L}_1 + \mathcal{L}_G + \mathcal{L}_P + \mathcal{L}_I$ and $\mathcal{L}_{Multi-AP-GAN}$.

Besides the ROC curves, we also show the visual results for each experimental setting in Fig. 12. Given the input Polar image, the synthesized results from different experimental settings are shown in Fig. 12. It can be observed that \mathcal{L}_1 captures the low-frequency features of images very well. $\mathcal{L}_1 + \mathcal{L}_G$ can capture both low-frequency and high-frequency features in the image. However, it adversely introduced distortions and artifacts in the synthesized image. In addition, optimizing $\mathcal{L}_P + \mathcal{L}_I$ suppresses these distortions to some extent. Finally, fusing attributes into the loss (i.e. $\mathcal{L}_{Multi-AP-GAN}$) can

not only improving the performance but also preserves facial attributes

In addition, we analyze the effect of attributes on the synthesized images in Figure 13. In particular, given the input gallery image, we examine how attributes help in synthesizing a visible image from a thermal probe image. If the probe image and the input gallery image share the same identity then Multi-AP-GAN is able to generate attribute preserving visible image. On the other hand, if the probe image's identity is different from that of the gallery image then the proposed method is not able to synthesize identity preserving visible face. However, the attributes are still preserved on the synthesized image.

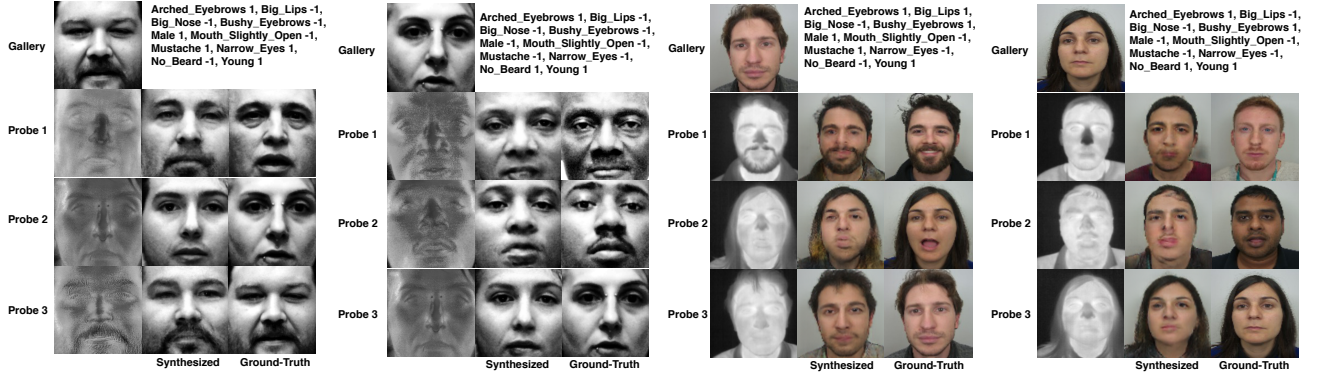


Fig. 13: Analysis of attributes on synthesis. We show the synthesis samples from either conventional or polarimetric thermal images on both datasets. Given probe (thermal) images and estimated attributes from the gallery (visible) image, our proposed method can generate attribute preserving (visible) images.

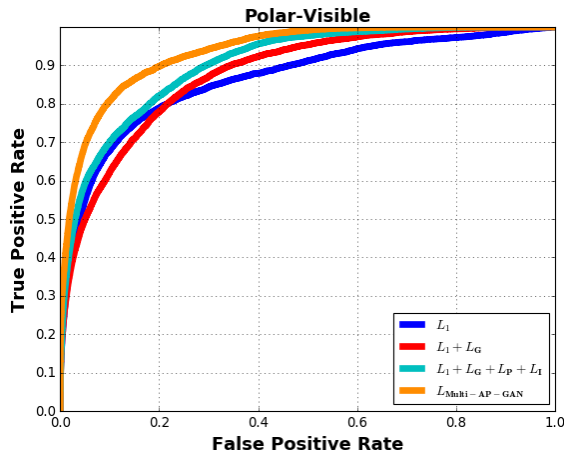


Fig. 14: The ROC curves corresponding to the ablation study.

This analysis further demonstrates that the proposed Multi-AP-GAN method learns the cross-spectral (thermal-to-visible) translation mapping exactly guided by the visual attributes.

VI. CONCLUSION

We propose a novel Attribute Preserving Generative Adversarial Network (Multi-AP-GAN) structure for thermal-to-visible face verification via synthesizing photo realistic visible face images from the corresponding thermal (polarimetric or conventional) images with extracted attributes. Rather than use only image-level information for synthesis and verification, we take a different approach in which semantic facial attribute information is also fused during training and testing. Quantitative and visual experiments evaluated on a real thermal-visible dataset demonstrate that the proposed method achieves state-of-the-art performance compared with other existing methods. In addition, an ablation study is developed to demonstrate the improvements obtained by different combination of loss functions.

ACKNOWLEDGMENT

This work was supported by the Defense Forensics & Biometrics Agency (DFBA). The authors would like to thank Mr.

Tom Cantwell and Ms. Michelle Giorgilli for their guidance and extensive discussions on this work. The authors would like to express their appreciation to ODNI/IARPA, as well as Chris Nardone, Marcia Patchan, and Stergios Papadakis at the JHU Applied Physics Laboratory for enabling ARL's participation in the 2018 IARPA Odin Program data collection, and Mathew Thielke for his help in collecting the data.

REFERENCES

- [1] D. Berthelot, T. Schumm, and L. Metz. Began: boundary equilibrium generative adversarial networks. *arXiv preprint arXiv:1703.10717*, 2017.
- [2] T. Bourlai, N. Kalka, A. Ross, B. Cukic, and L. Hornak. Cross-spectral face verification in the short wave infrared (swir) band. In *Pattern Recognition (ICPR), 2010 20th International Conference on*, pages 1343–1347. IEEE, 2010.
- [3] J. C. Chen, V. M. Patel, and R. Chellappa. Unconstrained face verification using deep cnn features. In *2016 IEEE Winter Conference on Applications of Computer Vision (WACV)*, pages 1–9, March 2016.
- [4] J. Deng, J. Guo, N. Xue, and S. Zafeiriou. Arcface: Additive angular margin loss for deep face recognition. In *Proceedings of the IEEE Conference on Computer Vision and Pattern Recognition*, pages 4690–4699, 2019.
- [5] X. Di and V. M. Patel. Face synthesis from visual attributes via sketch using conditional vaes and gans. *arXiv preprint arXiv:1801.00077*, 2017.
- [6] X. Di, B. S. Riggan, S. Hu, N. J. Short, and V. M. Patel. Polarimetric thermal to visible face verification via self-attention guided synthesis. In *2019 International Conference on Biometrics (ICB 2019)*, 2019.
- [7] X. Di, H. Zhang, and V. M. Patel. Polarimetric thermal to visible face verification via attribute preserved synthesis. In *2018 IEEE 9th International Conference on Biometrics Theory, Applications and Systems (BTAS)*, pages 1–10. IEEE, 2018.
- [8] A. Fukui, D. H. Park, D. Yang, A. Rohrbach, T. Darrell, and M. Rohrbach. Multimodal compact bilinear pooling for visual question answering and visual grounding. In *Proceedings of the 2016 Conference on Empirical Methods in Natural Language Processing, EMNLP 2016, Austin, Texas, USA, November 1-4, 2016*, 2016.
- [9] Y. Gao, O. Beijbom, N. Zhang, and T. Darrell. Compact bilinear pooling. In *Proceedings of the IEEE Conference on Computer Vision and Pattern Recognition*, pages 317–326, 2016.
- [10] I. Goodfellow, J. Pouget-Abadie, M. Mirza, B. Xu, D. Warde-Farley, S. Ozair, A. Courville, and Y. Bengio. Generative adversarial nets. In *Advances in neural information processing systems*, pages 2672–2680, 2014.
- [11] K. P. Gurton, A. J. Yuffa, and G. W. Videen. Enhanced facial recognition for thermal imagery using polarimetric imaging. *Opt. Lett.*, 39(13):3857–3859, Jul 2014.
- [12] R. He, J. Cao, L. Song, Z. Sun, and T. Tan. Adversarial cross-spectral face completion for nir-vis face recognition. *IEEE Transactions on Pattern Analysis and Machine Intelligence*, 2019.
- [13] R. He, X. Wu, Z. Sun, and T. Tan. Learning invariant deep representation for nir-vis face recognition. In *Thirty-First AAAI Conference on Artificial Intelligence*, 2017.

- [14] R. He, X. Wu, Z. Sun, and T. Tan. Wasserstein cnn: Learning invariant features for nir-vis face recognition. *IEEE transactions on pattern analysis and machine intelligence*, 41(7):1761–1773, 2018.
- [15] S. Hu, J. Choi, A. L. Chan, and W. R. Schwartz. Thermal-to-visible face recognition using partial least squares. *JOSA A*, 32(3):431–442, 2015.
- [16] S. Hu, N. J. Short, B. S. Riggan, C. Gordon, K. P. Gurton, M. Thielke, P. Gurram, and A. L. Chan. A polarimetric thermal database for face recognition research. In *Proceedings of the IEEE Conference on Computer Vision and Pattern Recognition Workshops*, pages 119–126, 2016.
- [17] P. Isola, J.-Y. Zhu, T. Zhou, and A. A. Efros. Image-to-image translation with conditional adversarial networks. *CVPR*, 2017.
- [18] J. Choi, S. Hu, S. S. Young, L. S. Davis. Thermal to visible face recognition. In *Proc.SPIE*, pages 8371 – 8371 – 10, 2012.
- [19] J. Johnson, A. Alahi, and L. Fei-Fei. Perceptual losses for real-time style transfer and super-resolution. In *European Conference on Computer Vision*, pages 694–711. Springer, 2016.
- [20] D. P. Kingma and J. Ba. Adam: A method for stochastic optimization. *arXiv preprint arXiv:1412.6980*, 2014.
- [21] B. Klare and A. K. Jain. Heterogeneous face recognition: Matching nir to visible light images. In *Pattern Recognition (ICPR), 2010 20th International Conference on*, pages 1513–1516. IEEE, 2010.
- [22] B. F. Klare and A. K. Jain. Heterogeneous face recognition using kernel prototype similarities. *IEEE transactions on pattern analysis and machine intelligence*, 35(6):1410–1422, 2013.
- [23] C.-Y. Lee, S. Xie, P. Gallagher, Z. Zhang, and Z. Tu. Deeply-supervised nets. In *Artificial intelligence and statistics*, pages 562–570, 2015.
- [24] J. Lezama, Q. Qiu, and G. Sapiro. Not afraid of the dark: Nir-vis face recognition via cross-spectral hallucination and low-rank embedding. In *2017 IEEE Conference on Computer Vision and Pattern Recognition (CVPR)*, pages 6807–6816. IEEE, 2017.
- [25] A. Mahendran and A. Vedaldi. Understanding deep image representations by inverting them. In *IEEE Conference on Computer Vision and Pattern Recognition, CVPR 2015, Boston, MA, USA, June 7-12, 2015*, pages 5188–5196, 2015.
- [26] K. Mallat and J.-L. Dugelay. A benchmark database of visible and thermal paired face images across multiple variations. In *International Conference of the Biometrics Special Interest Group, BIOSIG 2018, Darmstadt, Germany, September*, LNI, pages 199 – 206. GI / IEEE, 2018.
- [27] T. Miyato, T. Kataoka, M. Koyama, and Y. Yoshida. Spectral normalization for generative adversarial networks. In *International Conference on Learning Representations*, 2018.
- [28] F. Nicolo and N. A. Schmid. Long range cross-spectral face recognition: matching swir against visible light images. *IEEE Transactions on Information Forensics and Security*, 7(6):1717–1726, 2012.
- [29] O. M. Parkhi, A. Vedaldi, and A. Zisserman. Deep face recognition. In *Proceedings of the British Machine Vision Conference (BMVC)*, 2015.
- [30] N. Pham and R. Pagh. Fast and scalable polynomial kernels via explicit feature maps. In *Proceedings of the 19th ACM SIGKDD international conference on Knowledge discovery and data mining*, pages 239–247. ACM, 2013.
- [31] R. Ranjan, V. M. Patel, and R. Chellappa. Hyperface: A deep multi-task learning framework for face detection, landmark localization, pose estimation, and gender recognition. *IEEE Transactions on Pattern Analysis and Machine Intelligence*, pages 1–1, 2017.
- [32] R. Ranjan, S. Sankaranarayanan, A. Bansal, N. Bodla, J. C. Chen, V. M. Patel, C. D. Castillo, and R. Chellappa. Deep learning for understanding faces: Machines may be just as good, or better, than humans. *IEEE Signal Processing Magazine*, 35(1):66–83, Jan 2018.
- [33] S. Reed, Z. Akata, X. Yan, L. Logeswaran, B. Schiele, and H. Lee. Generative adversarial text to image synthesis. In *Proceedings of the 33rd International Conference on International Conference on Machine Learning - Volume 48, ICML’16*, pages 1060–1069. JMLR.org, 2016.
- [34] B. S. Riggan, N. J. Short, and S. Hu. Thermal to visible synthesis of face images using multiple regions. In *IEEE Winter Conference on Applications of Computer Vision (WACV)*, 2018.
- [35] B. S. Riggan, N. J. Short, S. Hu, and H. Kwon. Estimation of visible spectrum faces from polarimetric thermal faces. In *Biometrics Theory, Applications and Systems (BTAS), 2016 IEEE 8th International Conference on*, pages 1–7. IEEE, 2016.
- [36] O. Ronneberger, P. Fischer, and T. Brox. U-net: Convolutional networks for biomedical image segmentation. In *International Conference on Medical image computing and computer-assisted intervention*, pages 234–241. Springer, 2015.
- [37] F. Schroff, D. Kalenichenko, and J. Philbin. Facenet: A unified embedding for face recognition and clustering. In *Proceedings of the IEEE conference on computer vision and pattern recognition*, pages 815–823, 2015.
- [38] N. Short, S. Hu, P. Gurram, and K. Gurton. Exploiting polarization-state information for cross-spectrum face recognition. In *Biometrics Theory, Applications and Systems (BTAS), 2015 IEEE 7th International Conference on*, pages 1–6. IEEE, 2015.
- [39] N. Short, S. Hu, P. Gurram, K. Gurton, and A. Chan. Improving cross-modal face recognition using polarimetric imaging. *Optics letters*, 40(6):882–885, 2015.
- [40] N. Short, S. Hu, P. Gurram, K. Gurton, and A. Chan. Improving cross-modal face recognition using polarimetric imaging. *Opt. Lett.*, 40(6):882–885, Mar 2015.
- [41] K. Simonyan and A. Zisserman. Very deep convolutional networks for large-scale image recognition. *arXiv preprint arXiv:1409.1556*, 2014.
- [42] T. Bourlai, A. Ross, C. Chen, L. Hornak. A study on using mid-wave infrared images for face recognition. volume 8371, pages 8371 – 8371 – 13, 2012.
- [43] L. Wang, V. Sindagi, and V. Patel. High-quality facial photo-sketch synthesis using multi-adversarial networks. In *2018 13th IEEE international conference on automatic face & gesture recognition (FG 2018)*, pages 83–90. IEEE, 2018.
- [44] Y. Wen, K. Zhang, Z. Li, and Y. Qiao. A discriminative feature learning approach for deep face recognition. In *European Conference on Computer Vision*, pages 499–515. Springer, 2016.
- [45] X. Wu, R. He, Z. Sun, and T. Tan. A light cnn for deep face representation with noisy labels. *IEEE Transactions on Information Forensics and Security*, 13(11):2884–2896, 2018.
- [46] X. Wu, H. Huang, V. M. Patel, R. He, and Z. Sun. Disentangled variational representation for heterogeneous face recognition. In *Proceedings of the AAAI Conference on Artificial Intelligence*, volume 33, pages 9005–9012, 2019.
- [47] S. Xie and Z. Tu. Holistically-nested edge detection. In *Proceedings of the IEEE international conference on computer vision*, pages 1395–1403, 2015.
- [48] A. Yu, H. Wu, H. Huang, Z. Lei, and R. He. Lamp-hq: A large-scale multi-pose high-quality database for nir-vis face recognition. *arXiv preprint arXiv:1912.07809*, 2019.
- [49] H. Zhang, V. M. Patel, B. S. Riggan, and S. Hu. Generative adversarial network-based synthesis of visible faces from polarimetric thermal faces. In *IEEE International Joint Conference on Biometrics (IJCB)*, pages 100–107, Oct 2017.
- [50] H. Zhang, B. S. Riggan, S. Hu, N. J. Short, and V. M. Patel. Synthesis of high-quality visible faces from polarimetric thermal faces using generative adversarial networks. *International Journal of Computer Vision: Special Issue on Deep Learning for Face Analysis*, 2019.
- [51] H. Zhang, T. Xu, H. Li, S. Zhang, X. Wang, X. Huang, and D. Metaxas. Stackgan++: Realistic image synthesis with stacked generative adversarial networks. *arXiv preprint arXiv:1710.10916*, 2017.
- [52] K. Zhang, Z. Zhang, Z. Li, and Y. Qiao. Joint face detection and alignment using multitask cascaded convolutional networks. *IEEE Signal Processing Letters*, 23(10):1499–1503, Oct 2016.
- [53] T. Zhang, A. Wiliem, S. Yang, and B. C. Lovell. Tv-gan: Generative adversarial network based thermal to visible face recognition. *arXiv preprint arXiv:1712.02514*, 2017.
- [54] Z. Zhang, Y. Xie, F. Xing, M. McGough, and L. Yang. Mdnet: A semantically and visually interpretable medical image diagnosis network. In *Proceedings of the IEEE conference on computer vision and pattern recognition*, pages 6428–6436, 2017.
- [55] Z. Zhang, Y. Xie, and L. Yang. Photographic text-to-image synthesis with a hierarchically-nested adversarial network. In *Proceedings of the IEEE Conference on Computer Vision and Pattern Recognition*, pages 6199–6208, 2018.
- [56] H. Zhao, J. Shi, X. Qi, X. Wang, and J. Jia. Pyramid scene parsing network. In *Proceedings of the IEEE conference on computer vision and pattern recognition*, pages 2881–2890, 2017.
- [57] J.-Y. Zhu, T. Park, P. Isola, and A. A. Efros. Unpaired image-to-image translation using cycle-consistent adversarial networks. In *Computer Vision (ICCV), 2017 IEEE International Conference on*, 2017.